Physical Attributes of Single-Photon Tomography

Thomas F. Budinger

Donner Laboratory, Lawrence Berkeley Laboratory, University of California, Berkeley, California

Physical properties important for assessment of the potentials of emission computed tomography implemented by collimated detector systems include sensitivity, statistical and angular sampling requirements, attenuation compensation, resolution uniformity, and multisection design constraints. The limited angular range and sampling interval of coded aperture methods for longitudinal tomography impose severe limitations on quantitative imaging capabilities. These methods are discussed. Disadvantages of limited angular range are avoided by transverse section devices that have lower sensitivity than comparable positron devices. It is shown here, however, that the sensitivity for a single section device for head transverse section 2 cm thick can be $\simeq$200 events sec^{-1} μCi^{-1} per axial cm for 2 × 2 cm resolution. This is 40% of that for a well-designed positron system of similar resolution. The problem of attenuation compensation for constant attenuation, as in brain imaging, is well understood and a fast algorithm of the convolution type gives excellent results if angular sampling is over 360°.

Though there is a need to move the single-photon detector array over wide angular distances for adequate sampling, dynamic ECT is possible for the measurement of biological washout kinetics of clinical importance, such as clearance studies in brain. Based on physical principles, experiences with low sensitivity devices, and the prospects for devices with sensitivity comparable to positron tomographs, single photon tomography has sound potentials for research and clinical studies of the adult brain and whole body in small subjects. Practical whole-body tomography in adults is limited to nonquantitative lesion detection.

J Nucl Med 21: 579–592, 1980

The purpose of this paper is to present physical science aspects of emission tomography when collimators or coded apertures are used. Positron tomography involves electronic collimation and has properties that give it special advantages, particularly in imaging of the thorax and abdomen of adults. Nevertheless, there are important biological potentials of single-photon tomography because of the properties and availability of some of these radionuclides as well as the adequate sensitivity that can be obtained in studies of objects about 20 cm in diameter. A general explanation of tomography is given by describing four modes: multiple pinhole, time varying (stochastic) coded apertures, Fresnel coding, and computed transverse section tomography. In principle, all modes of tomography as well as the two contemporary classifications of longitudinal and transverse section tomography can be considered under the general topic of coded apertures wherein the code ranges from parallel hole collimators to arrays of irregularly spaced pinholes whose patterns change with time.

Received April 1, 1980; accepted April 1, 1980.

For reprints contact: Thomas F. Budinger, MD, PhD, Donner Laboratory, Lawrence Berkeley Laboratory, Univ. of California, Berkeley, CA 94720.

LONGITUDINAL TOMOGRAPHY

Pinhole arrays. The basic idea of longitudinal tomography can be shown by the moving pinhole aperture (Fig. 1). The image of two sources at different depths will appear shifted by amounts that are proportional to their depths and the amount the pinhole camera is displaced (P_x) from the original position. Because the block is

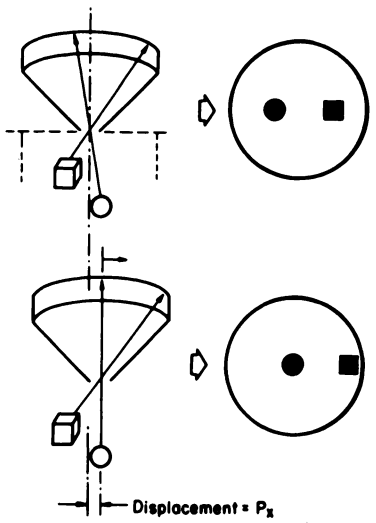

FIG. 1. Depth information is reflected by relative displacement of sources for different positions of pinhole aperture.

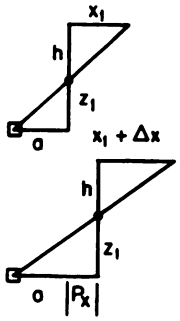

Initial Position

$$\frac{z_1}{a} = -\frac{h}{x_1} \text{ or } a = -\frac{z_1 x_1}{h} \quad (1)$$

After move

$$\frac{z_1}{P_x + a} = -\frac{h}{x_1 + \Delta x} \quad (2)$$

or

$$z_1 = \frac{-h P_x - h a}{x_1 + \Delta x}$$

Substitute eq 1

$$z_1 = -\frac{h P_x + z_1 x_1}{x_1 + \Delta x} \quad (3)$$

$$z_1 = -\frac{h}{\Delta x} P_x \quad (4)$$

FIG. 2. Relationship between amount of displacement and depth of source is derived by noting the similarity of triangles formed by ray optics.

closer to the aperture, the "block" image is displaced more than that of the "ball" image. The amount of image displacement is proportional to the ratio of the movement distance to the depth of the object and to the distance between the camera and the aperture. The relevant equations are derived by similarity of triangles as explained by Fig. 2.

Suppose there are a multitide of sources at various depths and positions; the images will represent the superposition of these sources, but their position and magnification will depend on the depth and planar position of these sources. If all of the sources were at depth Z_1, then the displacement of each source on each image

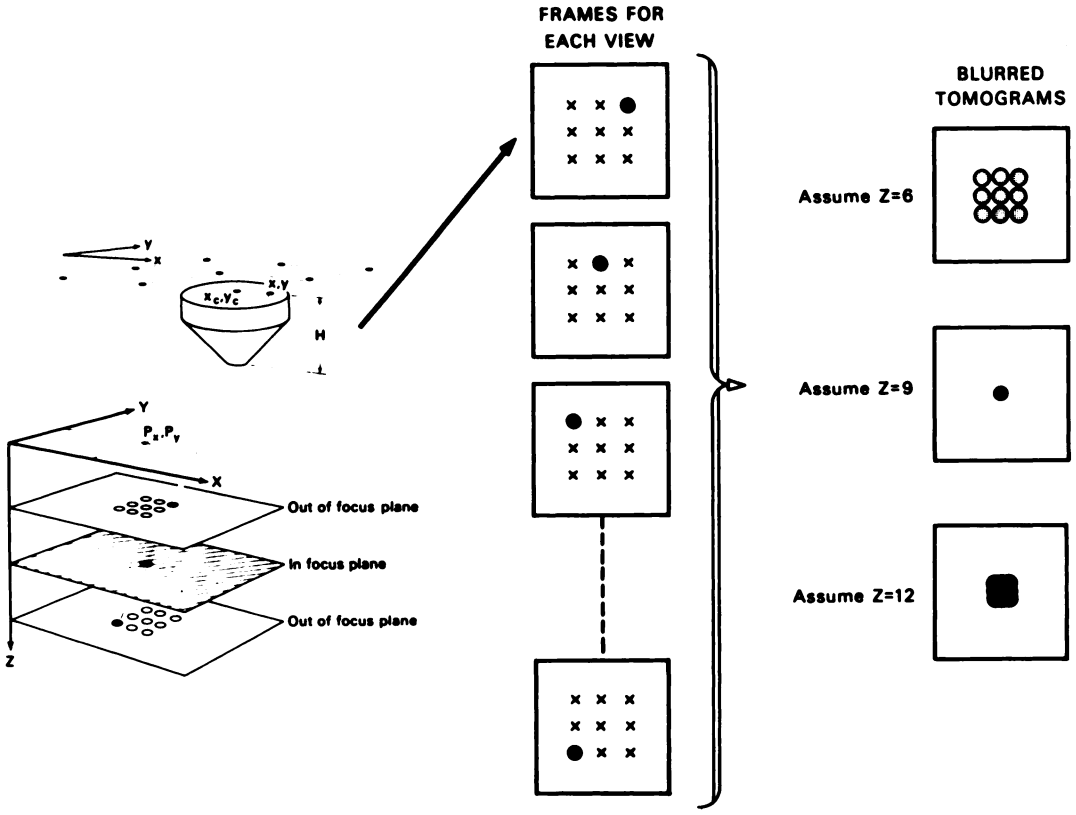

FIG. 3. Illustration of simple method of reconstituting the distribution at various planes by guessing at source depth and applying Eq. 1 to images taken for different aperture displacements (P_x,P_y).

would be described by

$$\Delta x = -\frac{H}{Z_1} Px_1,$$

$$\Delta y = -\frac{H}{Z_1} Py_1. \quad (1)$$

These equations are the rearrangement of terms from Eq. 4 in Fig. 2. Now let us shift back each picture element value to a new picture element for each displacement image in accord with Eq. 1. After this operation, we sum the resultant images to get a perfect image of the sources as if they were not displaced. However, suppose we erred in our estimate of the true depth Z_1 in Eq. 1, the result will be a blurred image of the sources, as demonstrated in Fig. 3 for one source at Z = 9 cm. Next, suppose we do not know at what depth the sources lie but guess at three successive depths and perform the operation of Eq. 1. The sources that happen to lie at the properly guessed depth will be in focus, whereas those at other depths will be out-of-focus. The blurred tomograms are similar to the simple backprojection images of transverse section computed tomography, and the basic data displayed by H. O. Anger's ingenious tomograph, which is now known as the Pho/Con tomograph (*1*). Digital implementation of tomography by multiple pinhole has been explored over the past 6 yr (*2*), and methods for deblurring these tomograms are discussed below.

One method is that of successive approximations, whereby the data in each image are corrected by factors derived from a comparison of the reprojected images with the observed images. The reprojections are obtained by simulating the imaging operation as if the backprojected images were the real data (Fig. 4). The data in the source space are adjusted until the differences between the reprojected images and the true images are small (*3*). This operation is similar to the early methods of computer assisted tomography, such as the arithmetic reconstruction technique (ART) (*4,5*), the orthogonal tangent correction method (*6*), the simultaneous iterative reconstruction (*7*), and the iterative least squares technique (*8*).

Stochastic coded aperture. A second class of multiple pinhole imaging is the stochastic coded aperture (*9,10*). Instead of moving an individual pinhole or providing many separate aperture (pinhole)-detector imaging chains, which look at the object from different directions as is done in the seven-pinhole system (*3*), the multiple aperture method collects the superposition of many pinhole views on each image. A sequence of images is recorded, each with a somewhat different arrangement of pinholes (Fig. 5). Suppose five images are taken, each with a uniquely different pinhole pattern. Recall that each pinhole represents a different angular view. After recording five images, we must "decode" the projection data that represent each angular view from the whole image series. To do so we solve the set of simultaneous equations shown in Fig. 5. In this particular case the angular view, A_1, corresponding to pinhole 1 projection

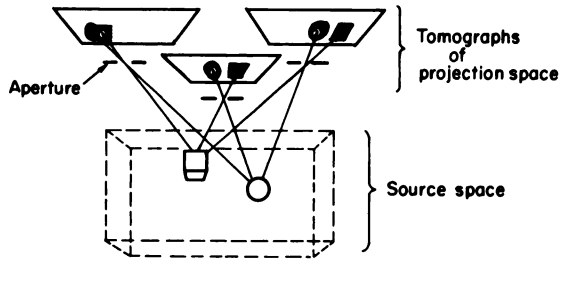

FIG. 4. Method of removing blur from multiple pinhole imaging system is to reproject simple superposition or backprojection images and make corrections to these images based on difference between reprojected images and actual data.

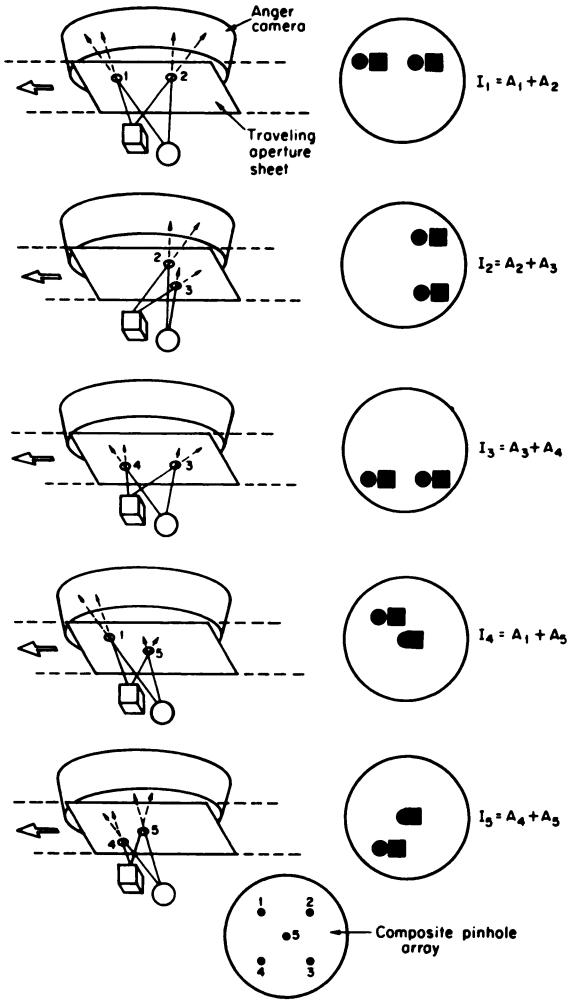

FIG. 5. Schematic of concept of stochastic aperture imaging wherein successive images are obtained, each representing different combination of views. By solving the set of simultaneous equations shown on right, information corresponding to particular aperture or angle can be "decoded."

only, is given by

$$A_1 = \frac{I_1 + I_3 + I_4 - I_2 - I_5}{2}$$
$$= \frac{(A_1 + A_2) + (A_3 + A_4) + (A_1 + A_5) - (A_2 + A_3) - (A_4 + A_5)}{2} \quad (2)$$
$$= A_1.$$

A_1 is the two dimensional (2D) pinhole projection image obtained from the object distribution viewed from the No. 1 aperture. After this decoding, we have data corresponding to various angular views and the reconstruction problem becomes similar to that for multiple pinhole systems or general computed tomography. This approach combines depth coding with good sensitivity because many apertures are "looking" at the subject at one time. Coded aperture techniques can be extended to complete angular sampling (*11*).

Another type of time varying, coded aperture imaging is digital computed tomography from images obtained using a rotation, slant-hole system similar in concept to the Anger tomoscanner. Recently, Chang and coworkers (*12*) designed a collimation system that has the advantages of multiple parallel hole projections without the geometric distortion of pinhole optics; yet, as will be shown, this system, as well as the contemporary multiple pinhole systems, has the disadvantages of limited angular range, and results are dependent on the orientation of the imaging system relative to the object.

Fresnel coded aperture. The Fresnel shadow image of radioactive sources is a series of concentric rings whose width and density depend on the source distance from the zone plate in a manner similar to the magnification of a pinhole aperture system. The tomograms can be calculated from a single image (Fig. 6) by varying the parameter R_1 in the algorithm (*13*).

$$(\mathcal{F}_2\, H(x,y)\exp\{-i\pi(x^2 + y^2)/R_1^2\}) \quad (3)$$

where $\mathcal{F}_2$ is the 2D Fourier transform and H(x,y) is the Fresnel shadowgram

R_1 = radius of the first ring

$$\times\left(1 + \frac{\text{zone plate to camera}}{\text{zone plate to object}}\right). \quad (4)$$

As with the multiple pinhole example, images obtained are blurred from underlying and overlying source data. Deblurring procedures similar to those outlined for the multiple pinhole procedures can be used here. The data are projections over a limited angular range, and the problems associated with limited angular range obtained here are as in the case for multiple pinhole and other coded-aperture imaging techniques.

Six problems associated with the longitudinal tomography techniques are: (a) noise propagation occurs during the decoding stage (e.g., the variance in A_1 data is the sum of the variances of each image); (b) attenuation compensation is complex and further amplifies er-

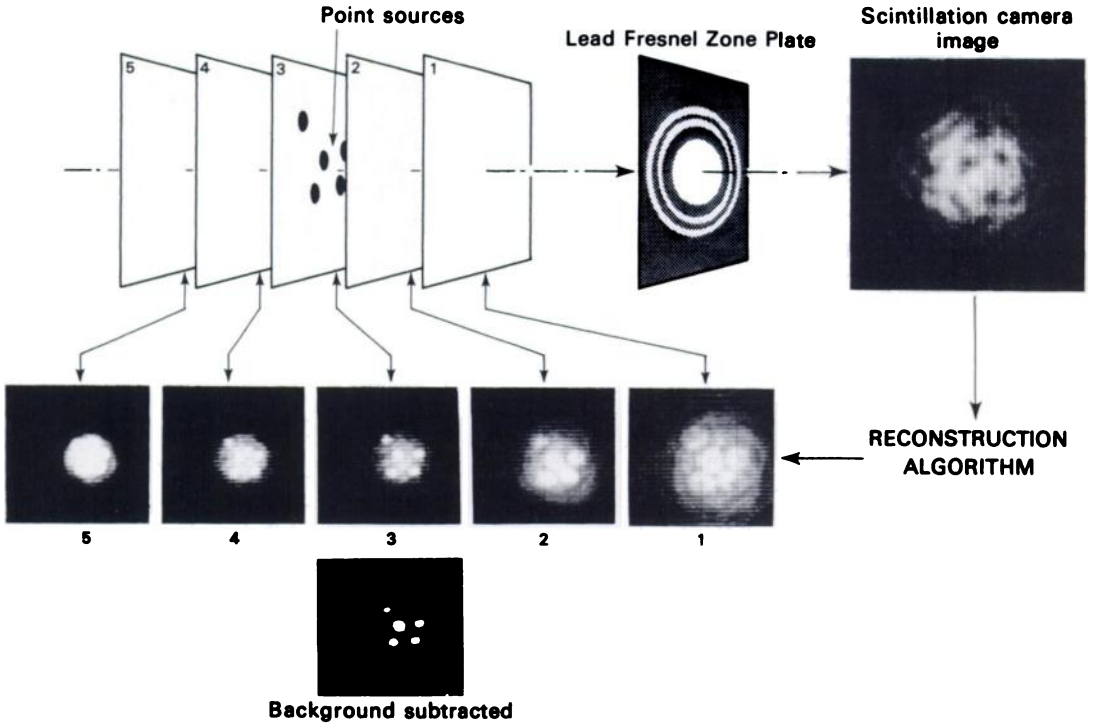

FIG. 6. The Fresnel aperture image consists of a series of concentric rings that project source information into detector. By varying phase relationships and Fourier transforming the shadowgram, longitudinal tomographs can be produced directly. These must subsequently be deblurred as with the multiple pinhole longitudinal tomograph data.

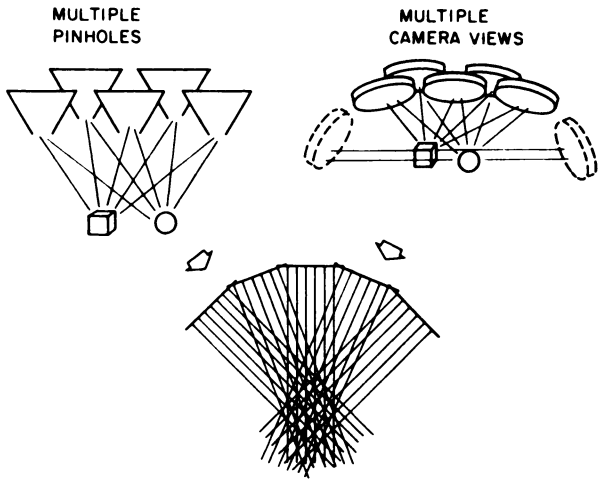

FIG. 7. Similarity between five pinhole views and five views using parallel collimator. Reorganization of the cone-beam data from pinholes can give a set of parallel rays closely corresponding to parallel set from conventional collimator.

rors; (c) the decoding calculation is tractable but computationally costly; (d) variable geometric magnification will cause distortion for pinhole systems; (e) a $\cos^3\theta$ sensitivity nonuniformity exists for pinhole systems; and (f) the data set lacks complete angular sampling.

The similarity between multiple pinhole imaging and transaxial computed tomography over limited angular range is shown in Fig. 7, and Figs. 8 and 9 illustrate the limitations imposed by collection of data over a limited angular range.

In view of the object orientation relative to the direction of angular sampling, it is clear that the results of a reconstruction are dependent on the shape and orientation of the object being reconstructed. The reason the seven pinhole technique gives such remarkably good images of the heart with only seven views over a limited angular range is in good part due to the symmetrical orientation of the detector array relative to the axis of the left ventricle's cylinder-like shape. Figure 9 shows that a change by only 20° in the axis of the detector array results in distortions, and a change by 90° results in imaging disaster. Sagittal or transverse sections are shown to illustrate the distortion problem and the magnitude of interplane errors due to the shape compared with the aperture orientation problem. When attenuation is added to the problem, even worse results are found. To give a fair evaluation of this aspect of longitudinal tomography over limited angular range, the author used the best available iterative reconstruction technique (conjugate gradient iterative least squares) with exact data and proper weighting for pixel geometry (*14*).

Methods of deblurring for limited angular sampling. Attempts to overcome the problem of limited angle in computed tomography by mathematical approaches have proceeded along two lines. One approach currently under evaluation is the use of the known deblurring operator that occurs between planes. This idea was formulated by Myers et al. (*15*) and subsequently was explored by others (*16–18*). These iterative or convolution approaches have the serious limitations shown in Figs. 8 and 9. To review, the problem of longitudinal tomography that uses projection data restricted to a limited angular range is that the reconstructed result is sensitive to the geometry of the object, the geometry of the viewing system, noise, and attenuation.

Some efforts have been directed toward incorporating *a priori* information about these factors into an algorithm for reconstruction tomography. For example, the convolution kernel or filter shape can be modified for each view in accord with the power spectrum or structure of the object as seen from that view and the noise characteristics of each view. The algorithm is a combination of the Weiner filter approach with the deblurring operation of computed tomography (*19*). For complete angular sampling this technique works very well, but it has

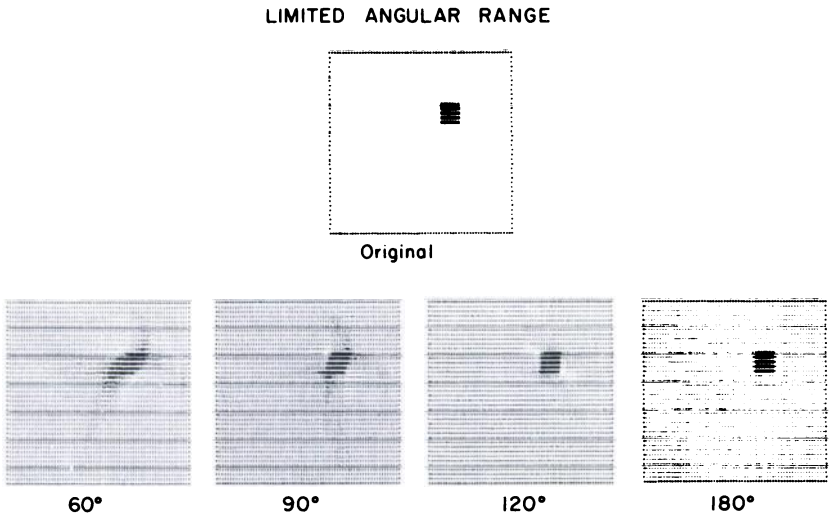

FIG. 8. The effect of projection data taken over limited angular range on fidelity of reconstruction is shown for square-shaped object. Results are dependent on orientation and shape of object relative to viewing direction.

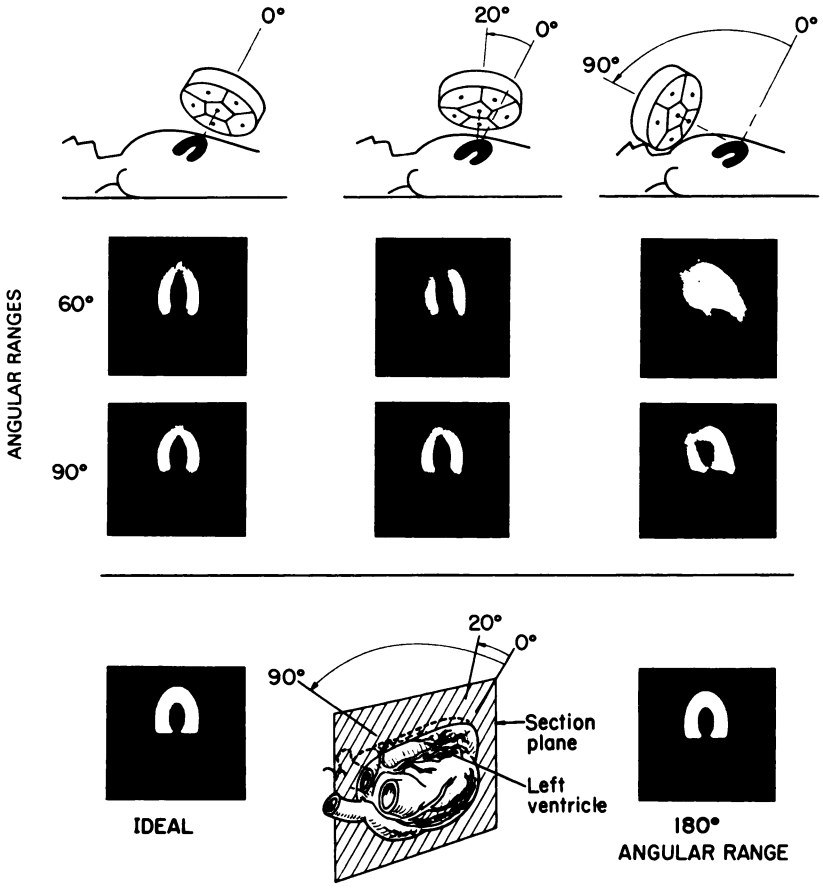

FIG. 9. Simulation of dependence of reconstructed result on orientation of a tomographic imaging system relative to multipinhole or parallel-hole system that has axis of symmetry of object. Angular sampling was limited to 60 and 90° for comparison with 180° of sampling without attenuation. Optical axis of imaging system is varied by 20 and 90° to demonstrate dependence of results on orientation of object relative to imaging axis.

not yet been investigated for the limited angular problem. A general approach that incorporates *a priori* information about the general shape or model to be reconstructed (e.g., rocket ship or human heart), as well as information about the geometry of the imaging system and the characteristics of the noise, is presented here for the interest of those who seek to solve the limited angle reconstruction problem.

Let the projections of a model distribution be given by $Hx' = p'$, where x' is the true model distribution. The image is

$$x = x' + H^{+}(p - p'), \tag{5}$$

where H^{+} is the Moore-Penrose generalized inverse of H. But for real data

$$x = x' + H^{+}(p - p') + H^{+}n. \tag{6}$$

The last term is noise and in many situations will dominate the reconstruction. Using a singular value decomposition of the pseudoinverse, we have

$$x = x' + \sum_{i=1}^{R} \lambda_i^{-1/2} V_i U_i^T \{p - p'\} + \sum_{i=1}^{R} \lambda_i^{-1/2} V_i U_i^T \{n\}. \tag{7}$$

where V_i are the eigenvectors of H^TH, and U_i are the eigenvectors of HH^T. The eigenvalues are λ_i. Terms in the first summation have magnitudes of comparable value; however, the terms in the second summation increase as $\lambda_i^{-1/2}$, since these eigenvalues are in order of decreasing magnitude. As more and more summations are used, the first term becomes smaller and smaller.

The summation is stopped when the signal-to-noise ratio becomes less than that expected from previously defined recipes. The success of this approach depends appreciably on our model of the noise and on how closely the assumed model of the object matches the true shape. Simulation with this algorithm using models that differ from the true distribution by the presence of large holes or sources show the technique has promise; however, at present the computational task is great, even on large computers. Of interest is the fact that iterative techniques, such as ART and least squares methods, can be correctly interpreted as methods to attempt to calculate Eq. 7 without forming the outer products directly. At present the best method to overcome the limited angle problem is to collect data over a wider angular range as is done in transverse section tomography.

The major advantage of coded aperture methods is that they hold some promise for dynamic emission tomography with single photons. An additional advantage

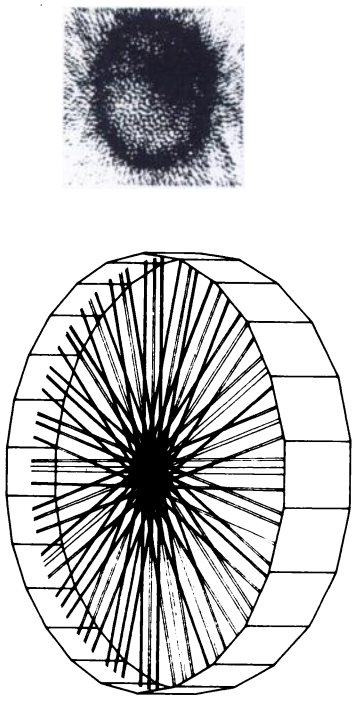

FIG. 10. Concept of transaxial computed tomography wherein views are taken around 360°. Image at right is simple superposition or backprojection of projection data from one level. Transactional-computed tomography involves mathematical techniques for removing blur of backprojected image similar to those used for longitudinal tomography.

is that longitudinal tomographic instrumentation can be adapted for computed tomography, though with available instrumentation the amount of imaging time required to give quantitative information is more than practical in most clinical situations. The statistical requirements for quantitative work will be presented below.

TRANSAXIAL COMPUTED TOMOGRAPHY

The concept of transaxial tomography has already been presented indirectly through the examples of how longitudinal tomography is implemented with coded apertures. The general concept of single photon computed tomography is shown in Fig. 10—a series of projections is made and these projections are then backprojected to form the superposition image. Figure 11 illustrates the methods used to acquire these data. As with the first step in computed longitudinal tomography, the backprojected image is blurred, and the deblurring objective is similar to that of longitudinal tomography. The contemporary implementation involves modifying or sharpening the projections before backprojecting. The mathematical methods have been discussed in general by Brooks et al. (*20*), and in detail for emission tomography by Budinger et al. (*21*). A major advantage of transaxial tomography over longitudinal computed tomography is the fact that 360° of data can be gathered by the devices shown in Fig. 11. Thus, transaxial tomography avoids the limited angle problem and allows more accurate compensation for attenuation.

Quantitative aspects. *Statistics.* The quantitative certainty of ECT is dependent on the number of detected events and the volume of interest. The act of reconstruction results in a propagation of noise that decreases the expected signal-to-noise ratio by factors of ten or more, depending on the resolution sought (Fig. 12). A TCT image represents about 10^9 detected events, whereas the usual ECT image is only 10^6 events. For ECT, the expected uncertainty is given as

$$\text{rms\%} = \frac{1.2 \times 100\ (\text{no. resolution cells})^{3/4}}{(\text{total no. events})^{1/2}}. \quad (8)$$

Figure 13 shows the relationship between detected events and volume of interest. The factor 1.2 is based on the convolution kernel. Therefore, if we collected 1.2×10^6 events for a section with 3000 pixels (400 events/pixel), the rms uncertainty is 44%. A naive prediction based on $\sqrt{N}/N \times 100$ would give only 5% uncertainty, but the situation improves if the activity is concentrated in a

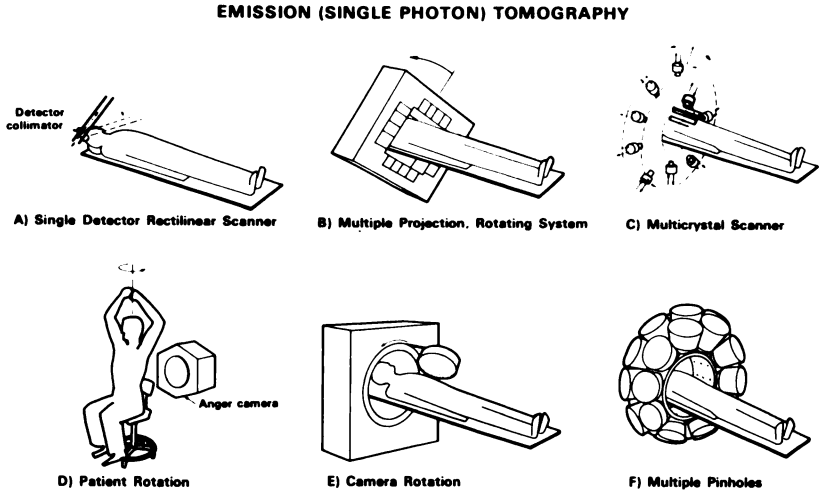

FIG. 11. Types of instrumentation that have been applied to transaxial-computed tomography. Multipinhole arrangement in 11F is theoretical construct that illustrates need for high sensitivity.

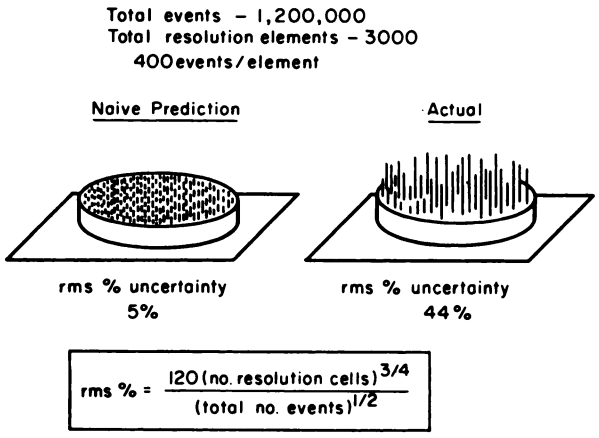

FIG. 12. Demonstration of magnitude of decrease in statistical reliability expected from projection image and that after computation of transverse section.

small region of the image. In the case of a single object in a uniform field (*22*):

$$\% \text{ rms uncertainty} = \frac{1.2 \times 100 \text{ (total no. events)}^{1/4}}{\left(\text{(average no. events per resolution cell in the target}\right)^{3/4}} \quad (9)$$

If the resolution cell size decreases by two, the required number of events for constant uncertainty increases by eight. Thus, an important goal for instrument design is to increase sensitivity (e.g., Fig. 11 F), and an important goal of reconstruction algorithms is to optimize resolution recovery and suppress noise artifacts.

Another aspect of noise propagation peculiar to ECT is the influence of errors in the attenuation coefficients used to correct the projection data before reconstruction (*23*). If variable attenuation coefficients are present in the region to be imaged, a transmission study is required to provide the attenuation coefficients. Because of the characteristics of ECT instrumentation, however, the transmission data are also of poor statistics. The propagation of errors due to these poor statistics in addition to the errors of the ECT procedure lead to great uncertainties in the images unless some method is used to incorporate *a priori* knowledge of the true value and distribution of the attenuation coefficients. Indeed, one can use the poor transmission data to determine the appropriate regions, such as lungs and heart, where known values of attenuation coefficients can be assigned. From this processed transmission image, the line integrals or weighting factors for attenuation compensation can be obtained.

Sensitivity. This section presents arguments to support the thesis that for head imaging, single photon tomographs can have a sensitivity only four times less than that of a single section positron tomograph. For multiple section devices and for objects of widths larger than 20 cm, the positron mode, however, has an even greater advantage over the single photon device.

A comparison of expected sensitivities for transverse section imaging of a 20 cm diameter head is shown in Fig. 14. The relation between detected counts and source intensity is

$$N_\gamma = \frac{\text{source activity} \times \text{crystal illumination area} \times \text{crystal efficiency} \times \text{effective attenuation}}{4\pi R^2} \quad (10)$$

For single photon imaging using the geometry of Fig. 14, the equation becomes:

$$N_\gamma = V \times \frac{(\rho S N_0) \times r \cdot S \times f \times \epsilon \times A}{4\pi R_1^2}, \quad (10)$$

where:

V = number of detector projection arrays;

ρ = μCi per axial cm;

S = section thickness (depending on collimator design the axial resolution distance might be two times the crystal illumination distance;

N_0 = 37,000 transformations sec^{-1} μCi^{-1} × no. useable photons per transformation;

r = transverse resolution;

f = packing fraction $(d/(d + t))^2$; see Fig. 14;

ϵ = crystal efficiency;

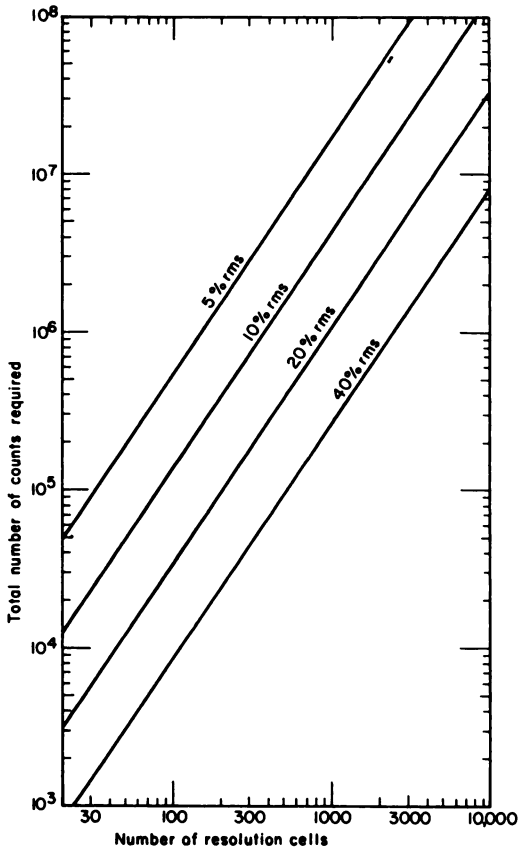

FIG. 13. Relationship between number of detected events and number of resolution elements in image for various degrees of statistical certainty.

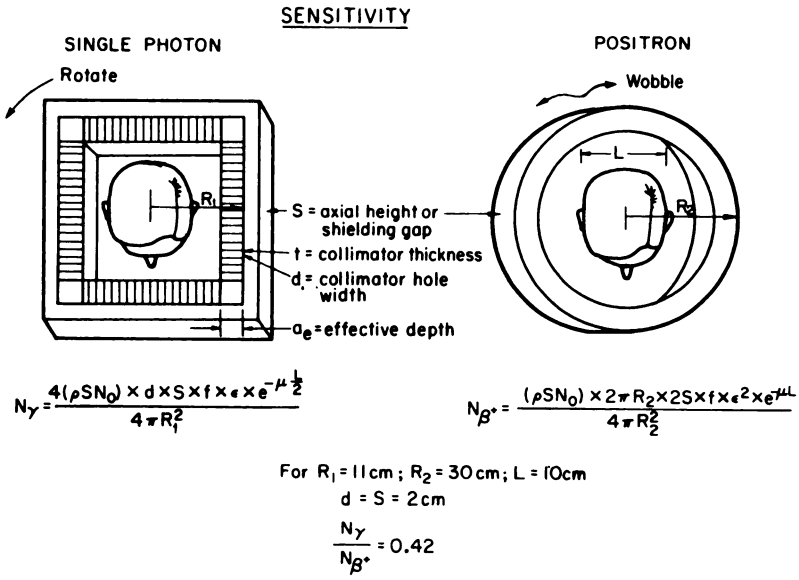

FIG. 14. Comparison of factors that determine sensitivities for single-photon and positron single-section tomographic devices collimator dimensions equated to 2 cm resolution for simplicity; see Eq. 10.

μ = attenuation coefficient;

A = effective attenuation (0.4 for 140 keV in a 20 cm diameter disc);

R_1 = distance from device center to the detectors.

A more detailed expression that incorporates explicitly the geometric optics of Anger (*24*) for a parallel channel collimator will give results similar to Eq. 10.

Using the following values: V = 4; S = 2.0 cm; r = 2.0 cm; f = 0.7; ϵ = 0.9; A = 0.4; R = 11 cm; Eq. 10 gives

$$N_\gamma = 196 \text{ counts sec}^{-1} \cdot \mu\text{Ci}^{-1} \text{ per axial cm.}$$

For positron annihilation photon imaging

$$N_{\beta^+} = \frac{(\rho SN_0) \times 2\pi R_2 \times 2S \times f \times \epsilon^2 \times A}{4\pi R_2}. \quad (11)$$

Comparison of Eq. 10 with Eq. 12 shows there is a sensitivity gain in the solid angle factor; however, this is offset by the fact that due to the coincidence detection requirements, the effective attenuation length is increased, and the crystal efficiency must be squared. Further, the exposed detector distance, S, is two times the section thickness. The need for side shielding to collimate or shield from activity outside the transverse section of interest gives a further reduction because of the need to increase R to accommodate this shield (*25*). Thus, for imaging a head 20 cm in diameter with 2 × 2 cm resolution, the parameters for the positron tomograph are: R_2 = 30, f = 0.95, ϵ^2 = 0.5, A = 0.2. Eq. 12 gives N_{β^+} = 469 annihilation events $\text{sec}^{-1} \cdot \mu\text{Ci}^{-1}$ per axial cm.

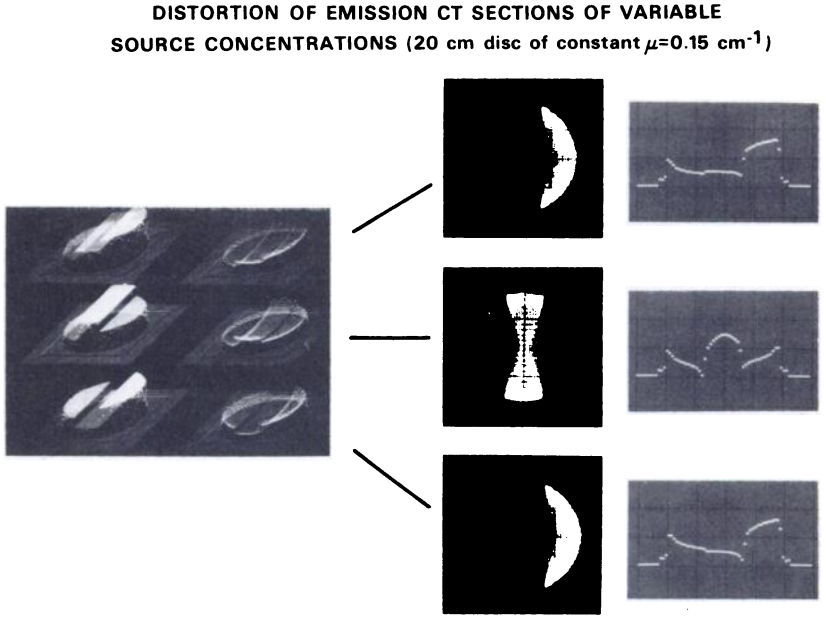

FIG. 15. Distortion of distribution in computed tomography of emission sources if attenuation is not adequately taken into account.

Thus the single photon system has 40% the sensitivity of a positron system. Unfortunately, the ratio of sensitivities is not constant for imaging larger objects, such as the thorax or abdomen. It changes with R for a positron system but with R^2 for a single photon system under contrast resolution conditions. The packing fraction decreases also.

The arguments above were made from another analytical viewpoint in a previous work in which we alluded to a five- or six-sided single photon system (*26*). As the number of detector arrays increases from four, the sensitivity decreases because of the need to increase R to accommodate the projection geometry. To obtain multiple angles the single photon device of Fig. 14 must rotate. In contrast, positron systems can provide multiple angles with little or no motion.

A second important qualification for this calculation is the fact that multiple section positron tomographs have a gain in sensitivity by a factor of $(3 - 2/N)$ over the single photon multisection device, where N is the number of axial detector arrays. This increase arises because the interplane coincidences give an additional plane with two times the sensitivity of the in-plane sensitivity.

Attenuation. A well-recognized difficulty in emission tomography is the fact that attenuation of the photons by tissue intervening between the source and the detector results in a serious distortion of the reconstructed images (Fig. 15). Although the methods of correcting for this attenuation error are conveniently implemented in positron tomography, the techniques are somewhat more cumbersome for single photon emission tomography. Nevertheless, over the past few years convenient methods have evolved using iterative approaches (*8,27*) and direct convolution techniques (*23,28,29*). Thus for situations of constant attenuation, the mathematical intractability has been overcome. Three methods are described below.

Modification of the geometric mean (*Method I*). The results of reconstructing projection data that have been modified by forming the geometric mean are better than those when no such maneuver is used; however, serious data distortion occurs (Fig. 15). By applying a correction factor that takes into account the thickness and average activity distribution (Fig. 16), it is possible to improve these results. The geometric mean of projection bin data is formed by multiplying opposing projection rays by one another, then taking the square root. To this modified projection value, a hyperbolic sine correction is applied, and then the convolution reconstruction method is used. The "sinh" correction factor is

$$\frac{e^x fx}{\sinh(x)} \qquad (12)$$

where x = attenuation coefficient × thickness/2 and f is set from 0.5 to 0.75 depending on the relative amount of activity along the projection line being modified. We

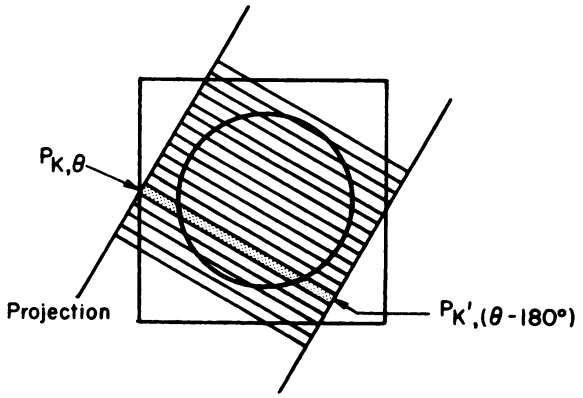

FIG. 16. Illustration of method of modifying geometric mean for attenuation compensation.

have had some success with this technique (*26*); however, the next two techniques give better results and are independent of the factor f. The method of finding the thickness of the object for each projection line involves estimation of the edges of the object from an initial reconstruction before applying the "sinh" correction.

Iterative modification of pixels (*Method II*). If an ECT reconstruction is performed without consideration of attenuation, the value of each pixel is low because the projected values were modified by an attenuation in accord with the distance between the pixel and the object edge along each ray that passes through that pixel. This modulation is given by $\exp(-\mu d_i)$ where d_i is the distance along a particular ray denoted by i (Fig. 17). The overall average modification of the source in a particular pixel is merely the sum of these separate modifications divided by the number of projections m:

$$\frac{1}{m}\sum_i e^{-\mu d_i}. \qquad (13)$$

The method of correction suggested by Chang (*27*) involves first performing a reconstruction to give the dis-

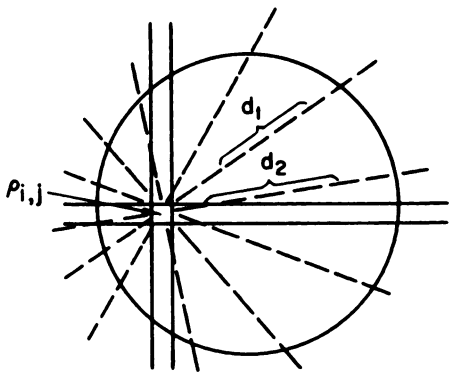

FIG. 17. Activity in a pixel i,j is detected as different event rates depending on distance between activity and edge of attenuating object. From analysis of average attenuation for all views, compensation for distortion of Fig. 15 can be made by iterative technique.

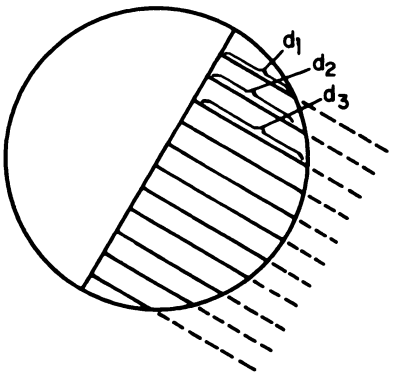

FIG. 18. First stage of method to modify each projection before application of special filter in implementing convolution-type of single photon emission computed tomography to compensate for attenuation involves modification of projection data by exp (diμ).

tribution $\rho_{i,j}^{old}$. Each pixel value $\rho_{i,j}$ is modified by

$$\rho_{i,j}^{new} = \rho_{i,j}^{old} \frac{1}{\frac{1}{m}\sum_i e^{-\mu d_i}}. \quad (14)$$

Then the modified data are reprojected and the differences between the reprojected bin values and the measured projections are determined. These "difference projections" are used to reconstruct an error image that, when added to the modified image, gives a good result for constant μ. Another iterative technique was proposed by Walters et al. (*30*). These techniques work well for objects, such as the head, which have constant attenuation coefficients.

Modification of bin values before convolution (Method III). This procedure has recently been developed by Gullberg (*23*) along lines suggested by Tretiak and Metz (*28*). First, bin values for each projection are multiplied by a factor $e^{+\mu d_k}$, where μ is the attenuation coefficient and d_k is defined in Fig. 18 as the distance from a center line to the object edge. Imagine a line through the axis of rotation and parallel to the projection array; the value of d_k is the distance between that line and the edge of the object. After modifying each value for every bin of each projection angle, the projection data are filtered by application of a filter whose shape is dependent on the attenuation coefficient and the resolution desired. The modified projection values are then backprojected into the image array after multiplication of each value by a factor related to the pixel distance from the center line. This procedure is very rapid, and the filter can be varied to accommodate different noise environments.

For variable attenuation coefficient situations, an iterative method in which the previously determined attenuation coefficients are used as weighting factors appears to be the only accurate method (*8,21*).

Uniformity of sensitivity and resolution. An important disadvantage of single-photon tomography is the nonuniformity of sensitivity for pinhole imaging and nonuniformity of resolution for parallel-hole collimation tomography (Fig. 19). Positron tomography does not share this problem. In single photon tomography it can be solved partially by forming the geometric mean (square root of the product of opposing rays), and then treating the data as parallel projections for an angular range of 180°. This method, however, is inferior to other techniques that require projections over 360° (*27,29*).

Other approaches for the resolution uniformity problem include use of collimators that give a uniform resolution over the range of the object (*31*), motion of the collimators (as in the Union Carbide scanner (*32*)), and incorporation of the spread function data in the reconstruction algorithm (*33*). Special collimators currently appear to be the most practical solution.

Multiple sections. Early work with multiple section single photon ECT was done on patients rotated with a large field-of-view Anger camera at Donner Laboratory (Fig. 20) (*8*). These and other studies (*34,35*) demonstrated that although the sensitivity of a single camera was only a few events per sec per μCi with the collimators we used, an inherent advantage was the simultaneous acquisition of multiple sections. Modern positron tomography will also have this capability and, due to the properties of electronic axial collimation, these tomographs will have an improved sensitivity over multisection single-photon devices.

A high sensitivity, single section, single-photon device, such as the Union Carbide scanner, cannot be extended easily to a multisection instrument because the crystal area used to gain the sensitivity obviates packing adjacent detector layers in the axial direction without large shielding gaps between layers.

Multiple angles. *Adequate sampling.* The need for rotation of the single photon detector or collimator units is an inherent problem, particularly when quantitative data requirements demand information from 360°. Data

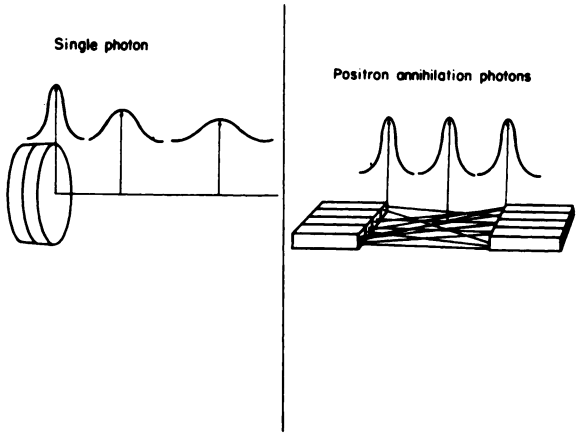

FIG. 19. Uniformity of resolution is generally poor with single photon tomographic systems unless special collimation is used.

distortion from limited angular sampling was shown in Figs. 8 and 9. Another type of distortion occurs when there is 360° coverage with an inadequate number of views (Fig. 21). Both of these sampling problems result in streaks and artifacts that are identified as the aliasing problem of under sampling (*36,37*).

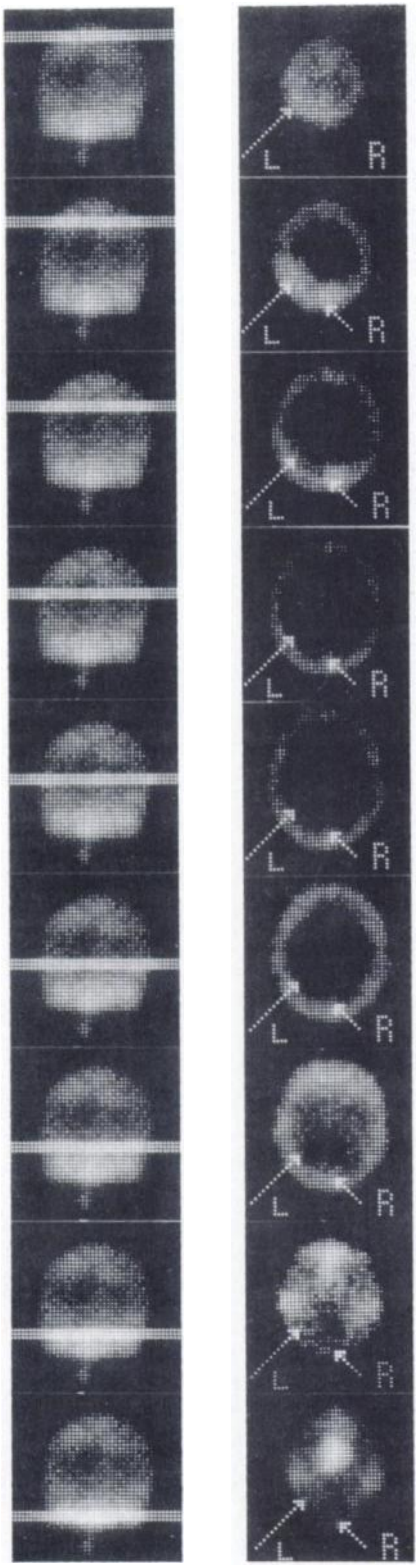

FIG. 20. Multiple sections of brain are obtained by sequentially reconstructing layers corresponding to levels in projected images for multiple view Anger camera studies. Shown is distribution of 10 mCi of Tc-99m pertechnetate in patient with brain tumors.

DYNAMIC ECT WITH SINGLE PHOTONS

Dynamic ECT refers to use of a time sequence of transverse sections from which uptake and washout ki-

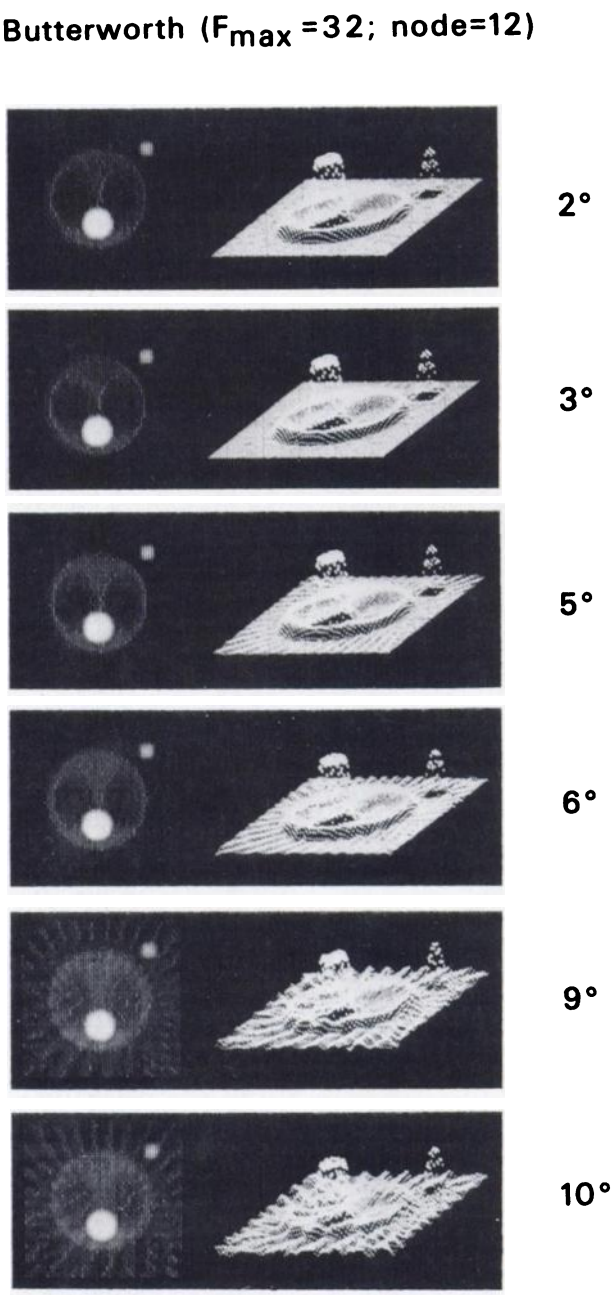

FIG. 21. Number of angular views necessary for 360° coverage in transverse section computed tomography is approximately equal to number of resolution elements across image. In this case for 64 resolution elements across image, aliasing artifact accompanying coarsely sampled data disappears for sampling with less than 5° increments.

netics can be deduced. The two major limitations to the application of dynamic computed tomography are the low statistics obtained and the necessity for rapid angular sampling. If motion of the detector assembly over about 45° is required, then imaging periods of about 10 sec are probably reasonable, and uptake kinetics might not be practical. Washout kinetics, however, such as clearance from brain, heart, and kidney, can be obtained using single photon devices with which one can collect more than 100,000 events in 1 min or less. A single photon system with four banks of detectors arranged as shown in Fig. 14 has been developed recently. This system has the requisite resolution and can perform dynamic washout studies after inhalation of Xe-133 or Xe-127 (*38*). The Kuhl Mark IV scanner has high sensitivity as well (*39*).

SUMMARY AND FUTURE PROSPECTS

Through both theoretical arguments and practical experience it has been shown that single photon computed tomography can provide a method of noninvasive quantitative imaging in animals and man. Because of the statistical requirements for quantitative investigations and the attenuation and solid angle problems for objects thicker than about 20 cm, it is concluded that the single photon instrumentation developments and applications should have a high likelihood for success in studies of the brain, but not of the thorax or abdomen of adults. Potential applications of single photon emission computed tomography in quantitative studies of the brain using acceptable doses include:

1. Brain blood volume using Tc-99m-labeled red cells (*40*).
2. Brain blood perfusion using I-123-iodoantipyrine (*41*) or other lipid soluble radiopharmaceuticals (*42*).
3. Brain perfusion studies using inhaled xenon-133 and xenon-127 (*38*).
4. Dopamine receptor site evaluation using I-123-phenethylamine radiopharmaceuticals.
5. Measurement of physiological conditions in the brain (*44*).

The quantitative potentials are based on obtainable sensitivities, the prediction of Eq. 8 or Fig. 13, and the percentage of the injected radiopharmaceutical that is available in the brain. If 2% of an injected dose of 10 mCi is present in the brain, we expect about 20 μCi per axial cm. A single photon system similar to that described in Refs. *38* and *39* can have a sensitivity of 50 events per second per axial cm for 1 cm × 1 cm resolution in sections 2 cm thick. Therefore, we can expect 1000 events per section or 1.2×10^5 events each 100 sec, adequate for ±20% quantitative accuracy. To achieve a ±20% accuracy in xenon washout studies where samples of 10–30 sec are required for flow measurement, the amount accumulated must be larger than 100 μCi or the resolution must be less. The quantitative volume for the case cited above is 2 cm × 2 cm (~2 times the resolution elements). The practicality of quantitative single photon imaging of the brain is based on the fact that many radiopharmaceuticals of interest in brain studies have an accumulation of 2–5% of the injected dose. Therefore, single photon ECT can be done at no significant radiation risk with injected doses of 10 to 20 mCi of Xe-133, Xe-127, Kr-81m, I-123, or Tc-99m radiopharmaceuticals.

The arguments of the paper do not exclude whole-body tomography as a useful tool for nonquantitative lesion detection.

ACKNOWLEDGMENTS

This paper benefited from discussions with Drs. Stephen Derenzo, Frank DeLand, Leonard Holman, John Keyes, W. Leslie Rogers, Robert Zimmerman, Gordon Brownell, David Kuhl, Grant Gullberg, Ronald Huesman, and Thomas Hill. This work was supported by the U.S. Department of Energy and and the National Institutes of Health.

REFERENCES

1. ANGER HO: Tomography and other depth discrimination techniques. In *Instrumentation in Nuclear Medicine,* vol. 2, Hine GJ, Sorenson JA, eds. New York, Academic Press, 1974, pp 61–100
2. MATHIEU L, BUDINGER TF: Pinhole digital tomography. In *Proceedings of the First World Congress of Nuclear Medicine,* Tokyo, 1974, pp 1264–1266
3. VOGEL RA, KIRCH D, LEFREE M, et al: A new method of multiplanar emission tomography using a seven pinhole collimator and an Anger scintillation camera. *J Nucl Med* 19: 648–654, 1978
4. GORDON R, HERMAN GT: Three-dimensional reconstruction from projections: a review of algorithms. *Int Rev Cytol* 38:111–151, 1974
5. OPPENHEIM BE: More accurate algorithms for iterative three-dimensional reconstruction. *IEEE Trans Nucl Sci* NS-21(3):72–77, 1974
6. KUHL DE, EDWARDS RQ, RICCI AR, et al: Quantitative section scanning using orthogonal tangent correction. *J Nucl Med* 14:196–200, 1973
7. GILBERT P: Iterative methods for the three-dimensional reconstruction of an object from projections. *J Theor Biol* 36: 105–117, 1972
8. BUDINGER TF, GULLBERG GT: Three-dimensional reconstruction in nuclear medicine emission imaging. *IEEE Trans Nucl Sci* NS-21(3):2–20, 1974
9. KORAL KF, ROGERS WL, KNOLL GF: Digital tomographic imaging with time-modulated pseudorandom coded aperture and Anger camera. *J Nucl Med* 16:402–413, 1975
10. KORAL KF, ROGERS WL: Application of ART to time-coded emission tomography. *Phys Med Biol* 24:879–894, 1979
11. WILLIAMS JJ, KNOLL GF: Initial performance of SPRINT: a single photon system for emission tomography. *IEEE Trans Nucl Sci* NS-26(2):2732–2735, 1979
12. CHANG W, LIN SL, HENKIN RE: A rotatable quadrant slant hole collimator for tomography (QSH): a stationary scintillation camera based spect system. Read before the Society of Nuclear Medicine Computer Council Meeting, Miami, Florida, 1980, in press
13. BUDINGER TF, MACDONALD B: Reconstruction of the Fresnel-coded gamma camera images by digital computer. *J Nucl Med* 16:309–313, 1975
14. HUESMAN RH, GULLBERG GT, GREENBERG WL, et al:

Users manual; Donner algorithms for reconstruction tomography. Berkeley, California, Lawrence Berkeley Laboratory PUB 214, October 1977

15. MYERS MJ, KEYES WI, MALLARD JR: An analysis of tomographic scanning systems. In *Medical Radioisotope Scintigraphy 1972,* vol. 1. Vienna, IAEA, 1973, pp 331-345
16. MACDONALD B, CHANG L-T, PEREZ-MENDEZ V, et al: Gamma-ray imaging using a Fresnel zone-plate aperture, multiwire proportional chamber detector, and computer reconstruction. *IEEE Trans Nucl Sci* NS-21:678-684, 1974
17. TOWNSEND D, PINEY C, JEAVONS A: Object reconstruction from focused positron tomograms. *Phys Med Biol* 23:235-244, 1978
18. BUDINGER TF: Three-dimensional imaging of the myocardium with isotopes. In *Cardiovascular Imaging and Image Processing, Theory and Practice 1975,* Harrison DC, Sandler H, Miller HA, eds. Palos Verdes Estates, California, Society of Photo-Optical Instrumentation Engineers, 1975, pp 263-271
19. TSUI ET, BUDINGER TF: A stochastic filter for transverse section reconstruction. *IEEE Trans Nucl Sci* NS-26(2): 2687-2690, 1979
20. BROOKS RA, DI CHIRO G: Principles of computer assisted tomography (CAT) in radiographic and radioisotopic imaging. *Phys Med Biol* 21:689-732, 1976 (review article)
21. BUDINGER TF, GULLBERG GT, HUESMAN RH: Emission computed tomography. In *Topics in Applied Physics, Vol. 32: Image Reconstruction from Projections; Implementation and Applications,* Herman GT, ed. Berlin, Springer-Verlag, 1979, pp 147-246
22. BUDINGER TF, DERENZO SE, GREENBERG WL, et al: Quantitative potentials of dynamic emission computed tomography. *J Nucl Med* 19:309-315, 1978
23. GULLBERG GT: The attenuated Radon transform: theory and application in medicine and biology, PhD Thesis, University of California, Berkeley, 1979. Lawrence Berkeley Laboratory, LBL-7486, 1979
24. ANGER HO: Sensitivity, resolution and linearity of the scintillation camera. *IEEE Trans Nucl Sci* NS-13:380, 1966
25. DERENZO SE, ZAKLAD H, BUDINGER TF: Analytical study of a high-resolution positron ring detector system for transaxial reconstruction tomograhy. *J Nucl Med* 16:1166-1173, 1975
26. BUDINGER TF, DERENZO SE, GULLBERG GT, et al: Emission computer assisted tomography with single-photon and positron annihilation photon emitters. *J Comput Assist Tomogr* 1:131-145, 1977
27. CHANG LT: A method for attenuation correction in radionuclide computed tomography. *IEEE Trans Nucl Sci* NS-25:638-643, 1978
28. TRETIAK OJ, METZ C: The exponential Radon transform. *Soc Ind Appl Math,* in press
29. GULLBERG GT, BUDINGER TF: Single-photon emission computed tomography; compensation for constant attenuation. *IEEE Trans Biomed Eng,* in press.
30. WALTERS TE, SIMON W, CHESLER DA, et al: Radionuclide axial tomography with correction for internal absorption. In *Information Processing in Scintigraphy,* Raynaud, C. Todd-Pokropek A, eds. Orsay, France, Comissariat à l'energie atomique, 1976, pp 333-342.
31. JASZCZAK RJ, CHANG L-T, STEIN NA, et al: Whole-body single-photon emission computed tomography using dual, large-field-of-view scintillation cameras. *Phys Med Biol* 24:1123-1143, 1979
32. STODDART HF, STODDART HA: A new development in single gamma transaxial tomography Union Carbide focused collimator scanner. *IEEE Trans Nucl Sci* NS-26(2): 2710-2712, 1979
33. ANSARI A, WEE WG: Reconstruction from projections in the presence of distortion. In *Proceedings of the 1977 IEEE Conference on Decision and Control,* Vol. 1. New Orleans, IEEE 77CH1269-OCS, 1977, pp 361-366
34. KEYES JW JR, ORLANDEA N, HEETDERKS WJ, et al: The humongotron—A scintillation-camera transaxial tomograph. *J Nucl Med* 18:381-387, 1977
35. JASZCZAK RJ, MURPHY PH, HUARD D, et al: Radionuclide emission computed tomography of the head with ^{99m}Tc and a scintillation camera. *J Nucl Med* 18:373-380, 1977
36. BUDINGER TF, DERENZO SE, GULLBERG GT, et al: Trends and prospects for circular ring positron cameras. *IEEE Trans Nucl Sci* NS-26(2):2742-2745, 1979
37. CRAWFORD CR, KAK AC: Aliasing artifacts in computerized tomography. *Appl Opt* 18(21):3704-3711, 1979
38. STOKELEY EM, SVEINSDOTTIR E, LASSEN NA, et al: A single photon dynamic computer assisted tomograph (DCAT) for imaging brain function in cross section. *J Comput Assist Tomogr,* in press.
39. KUHL DE, HOFFMAN EJ, PHELPS ME, et al: Design and application of Mark IV scanning system for radionuclide computed tomography of the brain. In *Medical Radionuclide Imaging,* vol. 1. Vienna, IAEA, 1979, pp 309-320
40. KUHL DE, ALAVI A, HOFFMAN EJ, et al: Local cerebral blood volume in head injured patients: determination by emission computed tomography of ^{99m}Tc-labelled red cells. *J Neurol Surg,* in press.
41. USZLER JM, BENNETT LR, MENA I, et al: Human CNS perfusion scanning with ^{123}I-iodoantipyrine. *Radiology* 115:197-200, 1975 (letter to the editor)
42. OLDENDORF WH: Need for new radiopharmaceuticals. *J Nucl Med* 19:1182, 1978
43. SARGENT TS, BUDINGER TF, BRAUN G, et al: An iodinated catecholamine congener for brain imaging and metabolic studies. *J Nucl Med* 19:71-76, 1978
44. KUNG HF, BLAU M: Regional intracellular pH shift; a proposed new mechanism for radiopharmaceutical uptake in brain and other tissues. *J Nucl Med* 21:147-152, 1980